III International Conference on Particle-based Methods – Fundamentals and Applications
PARTICLES 2013
M. Bischoff, E. Oñate, D.R.J. Owen, E. Ramm & P. Wriggers (Eds)

A DISCRETE ELEMENT MODEL FOR COHESIVE SOIL

Martin Obermayr[1*], Christos Vrettos[2], and Peter Eberhard[3]

[1] Fraunhofer Institute for Industrial Mathematics (ITWM)
Fraunhofer Platz 1
67659 Kaiserslautern, Germany
e-mail: martin.obermayr@itwm.fraunhofer.de,
web: http://www.itwm.fraunhofer.de/en

[2] Division of Soil Mechanics and Foundation Engineering
Technical University of Kaiserslautern
67663 Kaiserslautern, Germany

[3] Institute of Engineering and Computational Mechanics (ITM)
University of Stuttgart
Pfaffenwaldring 9, 70569 Stuttgart, Germany

Key words: discrete element method, cohesion, cohesive soil

Abstract. Soil can roughly be classified into cohesionless, cohesive, and cemented soil. In this contribution, a discrete element model for the simulation of cohesive soil is presented. It is based on a model for cohesionless material with spherical particles, normal repulsive and frictional contacts, as well as rolling resistance with an elastic limit to compensate the excessive particle rolling. The cohesive behavior is modeled by an additional attractive normal force between particles. The model is not derived from the microscopic origin of cohesion, such as liquid bridges or electrostatic forces. Instead, it is set up in analogy to the macroscopic shear failure characteristics of cohesive soil. It is observed in video inspections of a bulldozer blade operating in cohesive soil that after the cutting takes place the soil recovers more of its initial cohesion in areas of high compression. In areas away from the blade, the material behaves more like cohesionless soil, forming an angle of response. This behavior is reproduced by introducing a memory effect in the simulation. By that, the amount of cohesion is limited by the pressure that the contacting particles have experienced during the simulation. The discrete element model is shown to be scale invariant in the quasi-static regime, i.e. if all length scales of the model are scaled by a constant factor, the results remain unaffected by the scaling. The model is applied to a bulldozer blade pushing cohesive soil. The contact parameters are calibrated by simulated triaxial compression tests. A comparison between simulation and measurement shows good qualitative agreement.

1 INTRODUCTION

Soil can roughly be classified into cohesionless, cohesive, and cemented soil. Cohesionless soil includes all types of dry granular materials, such as dry sand and gravel. Curve (a) in Figure 1 on the left shows a typical stress–strain curve from triaxial compression tests for this case.

Sometimes, particles are held together by a bonding agent. Until bond breakage, the material behaves like an elastic solid. The stress–strain curve has a peak at low strains. Due to successively breaking bonds, the curve shows strain softening at post-peak and finally converges to the curve for the uncemented material at critical state. This is shown by curve (b) in Figure 1.

In contrast to the cementation, cohesion may be recovered when particles are separated and get in contact again. Cohesion has different physical origins including liquid bridges and electrostatic forces. The amount of cohesion caused by the different physical effects depends on the particles size. Regardless of its origin, cohesion causes an offset of the stress–strain curve, as shown in Figure 1, curve (c). In the same figure on the right, typical peak shear stress envelopes for different types of cohesion and cementation are plotted. The effect of cohesion and cementation on the shear stress envelop is similar. In both cases, the material develops a cohesive intercept. In case of cemented material, the shear stress envelope at critical state is identical with the uncemented material.

Models for cohesionless and cemented materials are given in [1] and [2], respectively. In this contribution, a discrete element model for cohesive soil is presented in Section 2. For completeness, also the cohesionless case is briefly described. This is necessary, because the cohesive model requires an additional attractive force on top of the cohesionless model. In Section 3 the scale invariance of the discrete element model is discussed. Finally, in Section 4, an application of the model to a bulldozer blade working in soil is presented.

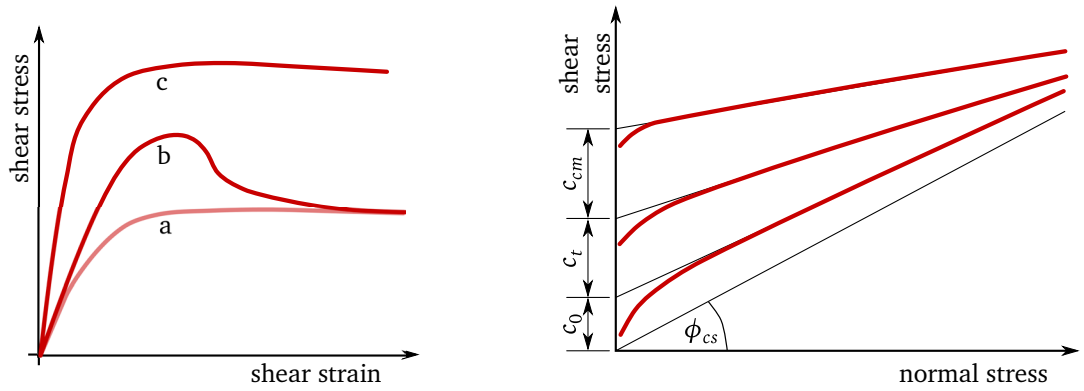

Figure 1: Effects of cementation on the response of a soil (left): a) cohesionless soil, b) cemented soil and c) cohesive soil or cemented soil at high normal effective stress. Peak shear stress envelopes for soils (right) resulting from cohesion c_o, soil tension c_t, and cementation c_{cm} (after [3]).

2 DISCRETE ELEMENT MODEL FOR COHESIVE SOIL

The focus of this contribution is on the model for cohesive material. The cohesive force is added to the forces from the cohesionless interaction. Thus, both models are presented in the subsequent sections.

2.1 Cohesionless soil

For the discrete element model presented in this section, only the force laws for the contacts between adjacent particles are given. The model has been implemented into Pasimodo, an object-oriented software platform for particle simulations [4]. This software provides all other necessary steps in the simulation, such as contact detection and time integration of the particle dynamics, and takes care of input and output operations. These steps are not detailed here.

2.1.1 Normal contact

In case of spherical particles, the overlap δ between contacting particles can be directly computed from their positions $\boldsymbol{x}_i$ and radii r_i and a repulsive contact force is calculated in case of $\delta > 0$. At the angle normal to the contact surface, a linear spring and dashpot model is applied

$$F_N = k_N \delta + d_N \dot{\delta} \tag{1}$$

with the normal stiffness $k_N = \frac{\pi}{2} \hat{E}\, \overline{r}$ and the damping coefficient d_N. In this formulation, the Young's modulus $\hat{E}$ of an imaginary rod with radius $\overline{r} = (r_1 + r_2)/2$ between the particle centers is the free parameter, see also [5]. In [2] it is shown, that this yields a scale independent model, which facilitates the practical usage.

2.1.2 Coulomb friction

As soon as two particles get in contact for the first time, the contact points on both particles, measured in their particle coordinate systems, are stored. If the contact points undergo a relative displacement, the contact points do not coincide any more in the successive simulation steps. In order to measure the tangential deformation, in every simulation step the contact points are transformed into the global coordinate system and the connecting vector of these two points $\boldsymbol{x}_{C,i}$, i.e.

$$\hat{\boldsymbol{\xi}}_T = \boldsymbol{x}_{C,2} - \boldsymbol{x}_{C,1} \tag{2}$$

is projected onto the tangential plane to get the tangential deformation vector $\boldsymbol{\xi}_T$. The tangential force is then computed from

$$\boldsymbol{f}_T = -k_T \boldsymbol{\xi}_T - d_T \dot{\boldsymbol{\xi}}_T \tag{3}$$

with the tangential stiffness k_T being a constant in this model, the tangential damping coefficient d_T, and the relative tangential velocity of the particles $\dot{\boldsymbol{\xi}}_T$. If the tangential force exceeds the limit $F_T = \mu\, F_N$, where μ is the local friction coefficient, slipping friction occurs. This is accounted for by resetting the tangential spring to

$$\boldsymbol{\xi}'_T = \frac{\mu\, F_N}{k_T} \frac{\boldsymbol{\xi}_T}{\|\boldsymbol{\xi}_T\|} \tag{4}$$

and updating the contact points accordingly, see [1] for more details.

2.1.3 Rolling resistance

When spherical particles with rotational degrees of freedom are used for the simulation of granular materials, the angle of internal friction is limited to very small values. If particles are not perfectly round, their common contact area may be flat, and so, allow for a torque transfer. In case of spherical particles, this effect has to be imitated by a rolling resistance torque. Increments of rolling deformations $\triangle\hat{\boldsymbol{\xi}}_R$ are computed from the contact points

$$\triangle\hat{\boldsymbol{\xi}}_R = \frac{\boldsymbol{x}_{C,2} + \boldsymbol{x}_{C,1}}{2} - \boldsymbol{x}_a \tag{5}$$

with the actuation point $\boldsymbol{x}_a = \boldsymbol{x}_1 + \frac{r_1}{r_2}(\boldsymbol{x}_2 - \boldsymbol{x}_1)$. The deformation increments are added to the accumulated rolling deformation vector from the last timestep

$$\hat{\boldsymbol{\xi}}_R^{(t=n)} = \boldsymbol{\xi}_R^{(t=n-1)} + \triangle\hat{\boldsymbol{\xi}}_R^{(t=n)}. \tag{6}$$

Then, the rolling deformation vector is transformed into the tangential plane. If the length of the rolling deformation vector exceeds the elastic limit, it is recomputed by

$$\boldsymbol{\xi}'_R = \frac{c_R\, \mu\, F_N}{k_T} \frac{\boldsymbol{\xi}_R}{\|\boldsymbol{\xi}_R\|}, \tag{7}$$

with the dimensionless rolling resistance coefficient c_R. Finally, a rolling resistance torque is computed from

$$\begin{aligned} \boldsymbol{t}_1 &= (\boldsymbol{x}_a - \boldsymbol{x}_1) \times (k_T\, \boldsymbol{\xi}_R) \\ \boldsymbol{t}_2 &= (\boldsymbol{x}_a - \boldsymbol{x}_2) \times (k_T\, \boldsymbol{\xi}_R) \end{aligned} \tag{8}$$

and applied to the particles.

2.2 Cohesive soil

On the macroscopic scale, cohesive materials are characterized by the fact that they have some shear strength even without confining pressure. This is described by a cohesive intercept c of the strength envelop as shown in Figure 1. The physical origins of cohesive behavior depend strongly on the size of the particles. The larger the particles, the lower

the influence of cohesion on the macroscopic properties. In the numerical simulation, the particles are scaled to control the numerical effort. A microscopic modeling of the cohesion, either dry or wet, is therefore considered as inappropriate. Nevertheless, in the following, a liquid bridge is used as model example for a cohesive particle interaction. Figure 2 shows a water bridge and the associated attractive pressure p_c. The attractive force F_c is the integral of the pressure over the particle surface. It raises the repulsive force F_N and, as a consequence, also increases frictional forces between particles.

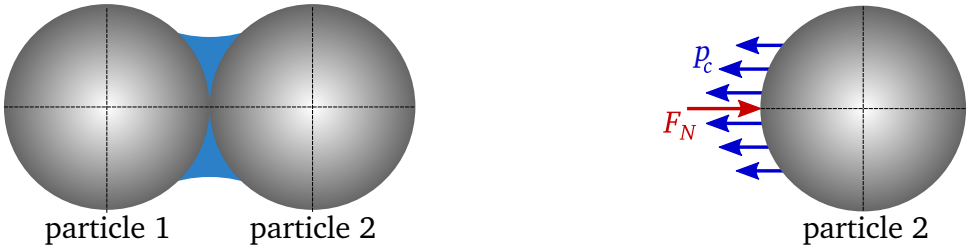

Figure 2: Capillary water and idealization as an attractive pressure p_c

The cohesive force appears whenever two particles get close enough to form a connection between the liquid coatings. This creation distance is denoted by the overlap δ_{cr} in Figure 3 on the left. The closer the particles are, the larger is the attractive force. As soon as the solid surfaces of the particles get in contact, the repulsive normal contact force F_N is activated, shown as a linear function of the overlap. Discrete element models for capillary cohesion that take into account the geometry of the liquid bridges, their volume and the distance of the particles are presented for example in [6].

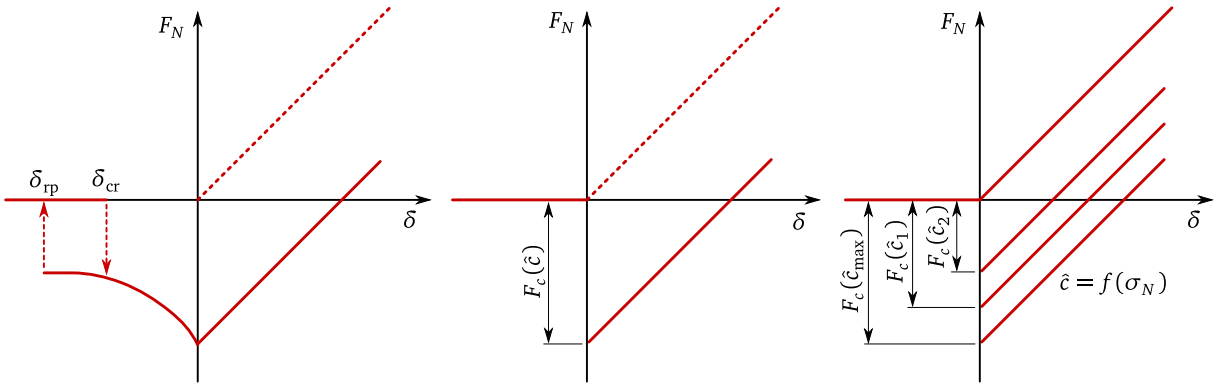

Figure 3: Normal contact force F_N vs. overlap δ for capillary water (left), constant cohesion (middle), and adaptive cohesion (right). The dashed lines refer to the force law for the cohesionless model.

A very simple model for cohesive granular material is applied in [7]. It mimics the macroscopic behavior of cohesive granular materials by a constant attractive force between

the particles, rather than the physical origin of the cohesion. The model has shown good qualitative agreements between simulation and measurement.

As an own adaption of this model, the normal contact model from Equation (1) is modified to include the cohesive force F_c

$$F_N = k_N\,\delta + d_N\,\dot{\delta} + F_c, \tag{9}$$

where the cohesive force is a function of the cohesive stress $\hat{c}$ and the average particle radius $\overline{r}$

$$F_c = \overline{r}^2\,\pi\,\hat{c}. \tag{10}$$

With the cohesive stress $\hat{c}$ being a constant, this model is called *constant cohesion*. The corresponding force law is shown in Figure 3 in the middle.

Own experiments with this model have revealed, that the material may behave too sticky if the full attractive force between particles is activated at once, when particles get in contact. Therefore, the cohesive stress is modified such that it accounts for the compressive stress that a pair of particles has experienced so far in the simulation. At the beginning of the simulation, an initial value $\hat{c}^{(t=0)} = \hat{c}_0$ is assigned. After that, new or recreated contact pairs start at zero cohesive stress. Depending on the compression between adjacent particles $\sigma_N = F_N/(\overline{r}^2\,\pi)$, the cohesive stress is then increased according to

$$\hat{c}^{(t=n)} = k_c \max\left(\sigma_N^{(t=1)}, \sigma_N^{(t=2)}, \ldots, \sigma_N^{(t=n-1)}\right). \tag{11}$$

At the same time, the cohesive stress is limited by its upper limit $\hat{c}_{\max}$. The model parameters are therefore $\hat{c}_0$, $\hat{c}_{\max}$, and k_c. The last parameter controls the amount of cohesion that is recreated by the normal force between particles. Each pair of particles has its own value for the current cohesive stress, which is updated in every timestep. This model is referred to as *adaptive cohesion*, see Figure 3 on the right. If soil is disturbed by a working tool, the cohesion can be recreated in areas of high pressure, e.g. at the bucket tip, while in areas of low pressure, the material remains in a loose state.

The Coulomb friction is only based on the repulsive part of the normal force F_N. This is indicated by the fact, that the cohesive force is drawn away from the contact point in Figure 2. In the implementation used here, this is respected by simply calculating the friction force before the cohesion is applied. Another option would be, to modify also the tangential force law in Equation (3) to include the cohesive intercept $\hat{c}$.

3 PARTICLE SCALING

In the numerical sample, the real grain size and grain size distribution cannot be approximated due to inherent numerical limitations. Thus particles have to be scaled by some factor in the simulation. If the numerical model is robust with respect to such scaling, the identification of the model parameters will be valid for different particle sizes, i.e. the particle size can be modified during the analysis without the need to identify a

new set of local contact parameters. According to [8], a contact law of the general form

$$F = k\,\overline{r}^{\alpha}\,\delta^{\beta} \tag{12}$$

with stiffness k, average particle radius $\overline{r}$, and overlap δ, is said to be scale invariant for three-dimensional problems, if

$$\alpha + \beta = 2. \tag{13}$$

While this condition is fulfilled for Hertzian contacts, with $\alpha = 1/2$ and $\beta = 3/2$, the usual form of the linear spring–dashpot model with a constant stiffness k_N is not scale invariant. In contrast to that, the linear model used here for unbonded particles is scale invariant, since $\alpha = 1$ and $\beta = 1$. Also the cohesive interaction is formulated in terms of stresses and thus expected to be scale invariant. In order to verify this, three simulations with identical parameters $\hat{E} = 100\,\mathrm{MPa}$, $k_T = 10\,\mathrm{kN/mm}$, $\mu = 0.3$, $c_R = 0.99$, and a lateral pressure of $\sigma_3 = 20\,\mathrm{kPa}$ are performed with scaling factors of 1, 10, and 100, respectively. All geometric quantities are scaled by this factor, i.e. the particle radii, their positions, and the dimensions of the container. All other values are kept unchanged. Figure 4 shows the stress–strain and volumetric curves for the original and the scaled models, confirming the mentioned scale invariance.

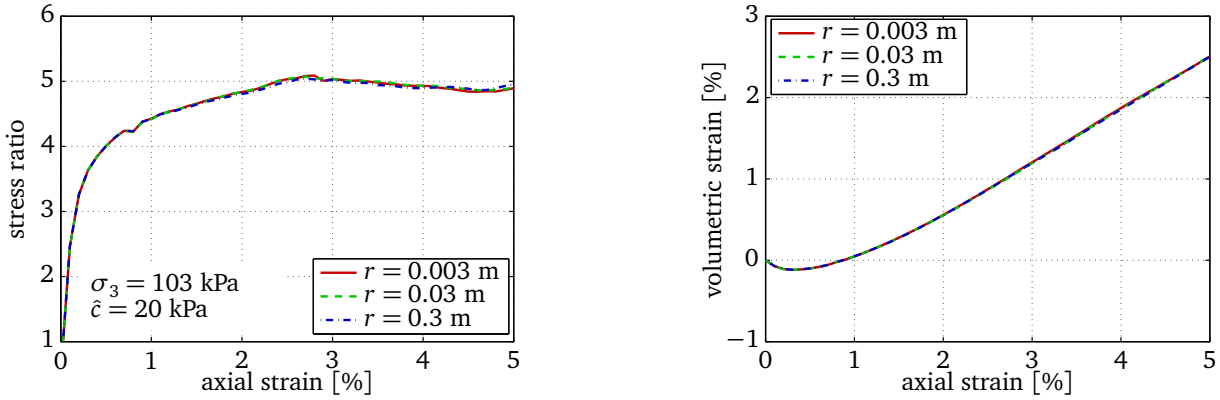

Figure 4: Stress ratio σ_1/σ_3 (left) and volumetric strain (right) vs. axial strain for simulated triaxial tests with scaled models of cohesive material with particle radii of $r = 0.003$, 0.03, and 0.3 m.

4 APPLICATION TO A BULLDOZING BLADE

In this section, the different simulation models, i.e. cohesionless, constant cohesion, and adaptive cohesion, are compared to measurements on a bulldozer blade with respect to the observed material flow. Measurements of the trajectory and video recordings of the material flow ahead of the blade are available. Although the comparison is only qualitative, the cohesive stress $\hat{c}$ is parameterized by triaxial compression tests in order to ensure that the model has realistic parameters.

4.1 Experimental setup

The experiments are performed on a 50 m track with natural cohesive soil with an angle of internal friction $\phi = 36.4\,^{\circ}$, cohesive intercept $c = 11.6\,\mathrm{kPa}$, bulk density $\rho_b = 1900\,\mathrm{kg/m^3}$, and an external friction coefficient between soil and blade of $\mu_{\mathrm{ext}} = 0.48$. The geometry of the blade is shown in Figure 5.

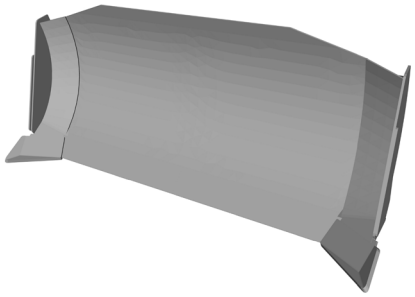

Figure 5: Geometry of the bulldozer blade.

The surface is leveled out by the bulldozer itself before the experiments. This preparation produces a surface that is not perfectly even. Thus, the actual elevation of the track is measured every 5 m before and after the experiment. From the difference of these two values, the cutting depth is calculated, see Figure 6. A wheel at the back of the bulldozer is used to record the forward speed. The forward position and cutting depth are shown in Figure 6. At the beginning, the bulldozer moves at a higher speed and scratches along the surface. At a cutting distance of about 10 m, the cutting depth increases and the speed goes down accordingly.

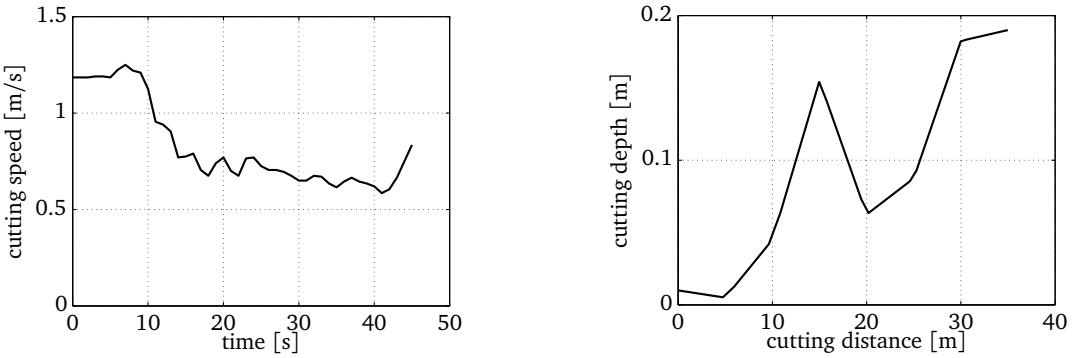

Figure 6: Forward position over time (left) and corresponding cutting depth (right).

4.2 Model setup

The simulation of a 5 m wide and over 40 m long track with a maximum particle size of 8 cm requires a numerical sample consisting of about $5 \cdot 10^5$ particles. This large number would make simulations of 45 s real-time very time consuming. In order to reduce the computational cost, symmetry is assumed with respect to a longitudinal vertical plane and only one half is modeled. Still, the number of particles is very large. Thus, particles behind the blade are fixed in space at a certain distance from the blade. This forms the boundary for the remaining particles. Then, at a larger distance from the blade, the already fixed particles are completely removed from the simulation.

The same procedure is applied in front of the blade. Not all of the particles are loaded at the beginning of the simulation, but slices of particles are successively read into the simulation. First, they are kept fixed in space and at a given distance from the blade, the particle dynamics is activated. By all that, the simulation contains only around 25000 active particles at a time. The simulation of 45 s real-time is achieved in about 62 hours on a single core, which relates to a real-time factor of a little less than 5000. This procedure is illustrated in Figure 7.

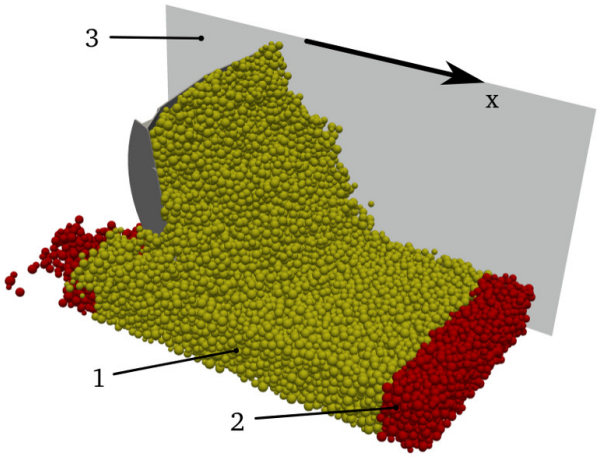

Figure 7: Setup of the numerical model with active particles 1), frozen particles 2), and symmetry plane 3). The arrow indicates the direction of travel x.

The particle interactions are composed of a repulsive linear law with Coulomb friction and rolling resistance for the cohesionless material, according to Equations (1), (3), and (8), respectively. Additionally, the cohesive force from Equation (10) is used with either a constant cohesive stress $\hat{c}$ or an adaptive cohesive stress from Equation (11). The parameterization is done by triaxial compression tests. Figure 8 shows the measured and simulated failure lines. The constant and adaptive cohesion models behave almost equal in the triaxial test. All parameters for the simulation are shown in Table 1.

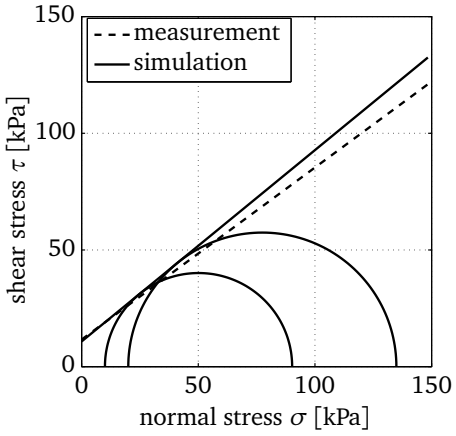

Figure 8: Triaxial test results.

Table 1: Parameters for the simulations.

parameter	**value**
particle radii r	$2 \ldots 4$ cm
normal stiffness $\hat{E}$	5 MPa
tangential stiffness k_T	$4 \cdot 10^5$ N/m
friction coefficient μ	0.27
soil–tool friction coefficient μ_{ext}	0.48
rolling resistance coefficient c_R	0.99
bulk density ρ_b	1900 kg/m^3
constant cohesion	
cohesive stress $\hat{c}$	35 kPa
adaptive cohesion	
initial cohesive stress $\hat{c}_0$	35 kPa
maximal cohesive stress $\hat{c}_{\max}$	35 kPa
proportionality factor k_c	0.1

4.3 Results

The purpose of this study is to investigate the difference between the two models for cohesion with respect to their capability to simulate a realistic flow pattern in front of the bulldozer blade. In Figure 9, snapshots of simulations with cohesionless material, constant and adaptive cohesion are shown. For the same simulations and at the same instant of time, in Figure 10 vector plots of the relative velocities between the particles and the bulldozer blade are shown. It is visible there, that the cohesionless material travels at the same velocity as the blade and forms an angle of response. The material is pushed upwards and then flows away along the sides of the blade. But in contrast to the cohesive materials, it does not form a "rolling" flow pattern.

The two cohesive models are very similar regarding their flow patterns at the area close to the blade. In both cases, the material flows upwards along the blade. Different to the cohesionless case, the material flows forward away from the blade on top of the heap. This causes a "rolling" motion of the material in front of the blade. For the constant cohesion, this circular flow pattern continues also for the downward motion, such that the overall motion is like a drum motion. In contrast to that, in case of the adaptive cohesion, the material trickles down on top of the heap. This is due to the lower cohesion at low confining pressures. A similar behavior has been observed in the natural material.

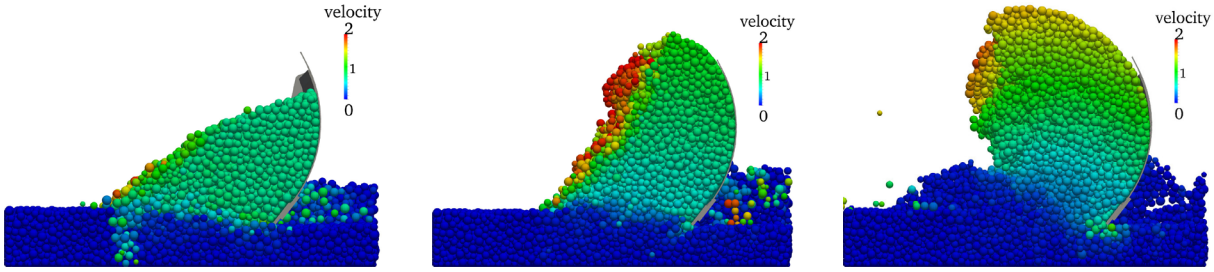

cohesionless adaptive cohesion constant cohesion

Figure 9: Snapshots of the simulations at time $t = 31s$. View from the symmetry plane.

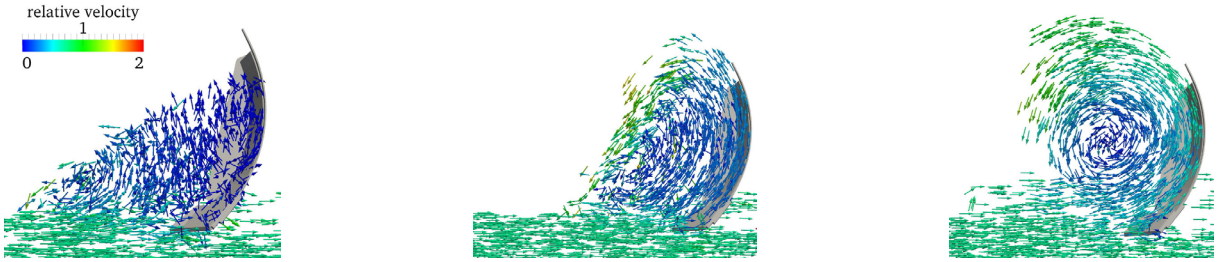

cohesionless adaptive cohesion constant cohesion

Figure 10: Relative velocities between particles and blade at time $t = 31s$, view from symmetry plane.

While both cohesive models are capable to reproduce a rolling flow pattern, the adaptive model reproduces the natural flow better than the constant model does. The cohesive stress $\hat{c}$ is selected according to the triaxial compression test and is equal in both models. But once a pair of particles has been separated, the actual cohesion depends on the amount of confining pressure in the adaptive model. Therefore, the material has a lower cohesion at the top layer than at the bottom.

Finally, snapshots from the simulation with the adaptive cohesion are compared to pictures from the test track in Figures 11 and 12. The amount of material in front of the blade increases in a similar manner in the simulation and measurement. The simulation shows a similar angle of response on the bottom of the heap. On the upper side, some material forms an overhang.

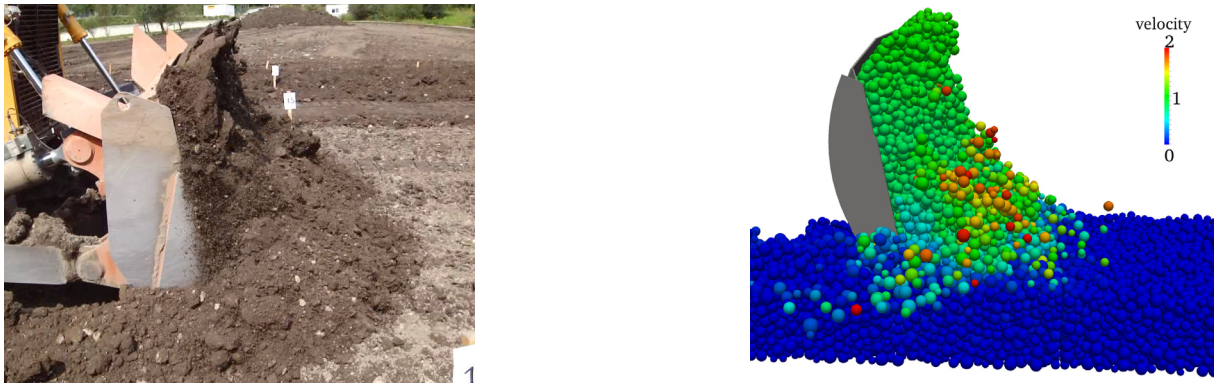

Figure 11: Comparison of the material flow in front of the bulldozer blade at $t = 16s$.

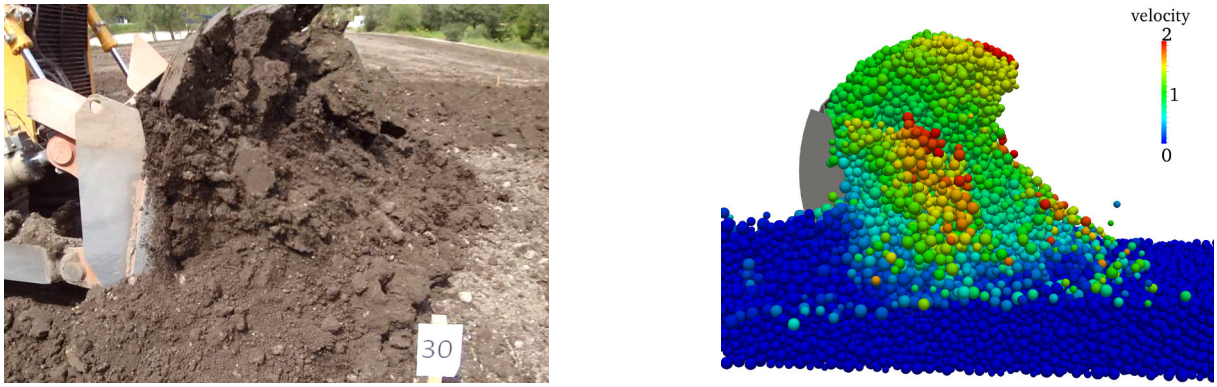

Figure 12: Compassion of the material flow in front of the bulldozer blade at $t = 37s$.

5 SUMMARY

In this contribution, a discrete element model for cohesive soil is presented. The model is not based on a specific micromechanical effect, such as liquid bridges or electrostatic forces. Instead, it allows to capture the macroscopic behavior of cohesive soil. The model is shown to be scale invariant, which facilitates the practical application. Comparison of the material flow in front of a bulldozer blade shows good qualitative agreement between the simulation and a measurement.

6 ACKNOWLEDGMENTS

This work was funded by the Fraunhofer Innovation Cluster *Digital Engineering for Commercial Vehicles*. The support of Dr. Claus Lamprecht from Liebherr for providing the measurements in Section 4 is gratefully acknowledged.

REFERENCES

[1] M. Obermayr, C. Vrettos, J. Kleinert, and P. Eberhard. A discrete element method for assessing reaction forces in excavation tools. In *Proceedings of the Congress on Numerical Methods in Engineering - CNM 2013*, Bilbao, Spain, June 2013.

[2] M. Obermayr, K. Dressler, C. Vrettos, and P. Eberhard. A bonded-particle model for cemented sand. *Computers and Geotechnics*, 49:299–313, 2013.

[3] M. Budhu. *Soil mechanics and foundations*. John Wiley & Sons, New York, 2007.

[4] F. Fleißner. *Parallel Object Oriented Simulation with Lagrangian Particle Methods*, volume 16 of *Schriften aus dem Institut für Technische und Numerische Mechanik der Universität Stuttgart*. Shaker, Aachen, 2010.

[5] C. Ergenzinger, R. Seifried, and P. Eberhard. A discrete element model to describe failure of strong rock in uniaxial compression. *Granular Matter*, 13(4):1–24, 2010.

[6] U. El Shamy and T. Gröger. Micromechanical aspects of the shear strength of wet granular soils. *International Journal for Numerical and Analytical Methods in Geomechanics*, 32(14):1763–1790, 2008.

[7] T. Tsuji, Y. Nakagawa, N. Matsumoto, Y. Kadono, T. Takayama, and T. Tanaka. 3-D DEM simulation of cohesive soil-pushing behavior by bulldozer blade. *Journal of Terramechanics*, 49(1):37–47, 2012.

[8] Y. T. Feng, K. Han, D. R. J. Owen, and J. Loughran. On upscaling of discrete element models: similarity principles. *Engineering Computations*, 26(6):599–609, 2009.